Uniwersytet Jagielloński w Krakowie

Wydział Fizyki, Astronomii i Informatyki Stosowanej

Kamil Rakoczy

Nr albumu: 1111020

Adaptation of image reconstruction algorithms with time-of-flight for the J-PET tomography scanner

Praca magisterska
na kierunku Informatyka Stosowana

Praca wykonana pod kierunkiem
dr inż. Wojciech Krzemień
Zespół Zakładów Fizyki Jądrowej

Kraków 2019

Acknowledgments

First of all, I would like to thank my thesis supervisor dr. inż. Wojciech Krzemień. Without his guidance and dedicated involvement in every step throughout the process, this paper would never have been accomplished.

Moreover I would like to thank prof. dr hab. Paweł Moskal for giving me the opportunity to be a part of the J-PET research group.

Also I would like to thank the whole J-PET team for given advises and discussions, especially I want to to thank dr inż. Lech Raczyński for his valuable suggestions and sharing his knowledge about image reconstruction.

Last but not least I would like to thank Asia, who shined my face with her smile each time I was overwhelmed with amount of work. I don't know if I would complete this work without you.

Abstract

The main aim of this thesis is the implementation of various analytic image reconstruction algorithms in the frame of the J-PET Framework analysis package. The implemented algorithms: Kernel Density Estimation, Filtered Back-Projection and Time-Of-Flight-Filtered Back-Projection have been tested both using Monte Carlo simulations and experimental data gathered by the scanner. Obtained results show that the implemented algorithms reconstruct correctly the shape of the phantoms. Comparison studies between implemented algorithms have been performed. In reconstruction of the NEMA phantom, the best results have been obtained using the Shepp-Logan filter with the cut-off parametr equal to 0.75 of Nyquist frequency (corresponding to the Background Variability of 0.13 and the Contrast Recovery Coefficient equal to 1.03 for high activity region of radius 22 mm). For the Time-of-Fligth Filtered Back-Projection algorithm, the best reconstruction was obtained using the Hamming filter with the cut-off parameter equal to Nyquist frequency (corresponding to the Background Variability of 0.17 and the Contrast Recovery Coefficient equal to 0.96 for high activity region of radius 22 mm).

Streszczenie (Abstract in Polish)

Głównym celem pracy jest zaimplementowanie analitycznych algorytmów rekonstrukcji obrazu w ramach pakietu oprogramowania J-PET. Zaimplementowane algorytmy: Kernel Density Estimation, Filtered Back-Projection and Time-Of-Flight-Filtered Back-Projection zostały przetestowane używając symulacji Monte Carlo, a także danych eksperymentalnych zarejestrowanych prototypem skanera J-PET. Przedstawione wyniki pokazują, że algorytmy rekonstruują poprawnie kształt fantomów. Dokonano studiów porównawczych zaimplementowanych algorytmów. Rekonstruując fantom NEMA, najlepsze wyniki zostały osiągnięte używając filtru Sheppa-Logana z parametrem częstotliwości odcięcia równym 0.75 częstotliwości Nyquista (Wariancja tła = 0.13, Kontrast obrazu = 1.03 dla obszaru kuli o wysokiej aktywności o promieniu 22 mm). Używając algorytmu Time-of-Fligth Filtered Back-Projection najlepszy wynik osiągnięto dla filtru Hamminga z parametrem częstotliwości odcięcia równym częstotliwości Nyquista (Wariancja tła = 0.17, Kontrast obrazu = 0.96 dla obszaru kuli o wysokiej aktywności o promieniu 22 mm).

Contents

Abbreviations

PET	Position emission tomography
CT	Computed tomography
LOR	Line-of-response
JPET	Jagiellonian PET
TOF-PET	Time-of-flight position emission tomograph
FBP	Filtered Back-Projection
TOF-FBP	Time-of-flight Filtered Back-Projection
DAQ	Data Acquisition System
FPGA	Field Programmable Gate Array
SiPM	Silicon Photomultiplier
MLEM	Maximum Likelihood Estimation Method
BP	Back-projection
TOF	Time-of-flight
KDE	Kernel Density Estimation
PPM	Portable Pixel Map
CI	Continuous Integration
NEMA	The National Electrical Manufacturers Association

List of Figures

1. Introduction

Position Emission Tomography (PET) is a non-invasive medical imaging technique that allows to study metabolic changes in human body. First clinically applicable PET scanner was created in 1975 by Phelps and Hoffman [6, 7]. Today the PET tomography still remains an important tool both in clinical applications and in research, used mainly in oncology and brain disease studies.

To perform PET scan, the radiotracer (such as fludeoxyglucose) is administered to the patient. Radiotracers emit positrons which annihilate with electrons from patients body. The e^+e^- masses are transformed into two 511 keV photons which are emitted with relative angle of almost 180-degree [1].

e^+ positron
e^- electron
ν neutrino
γ photon(511 keV)
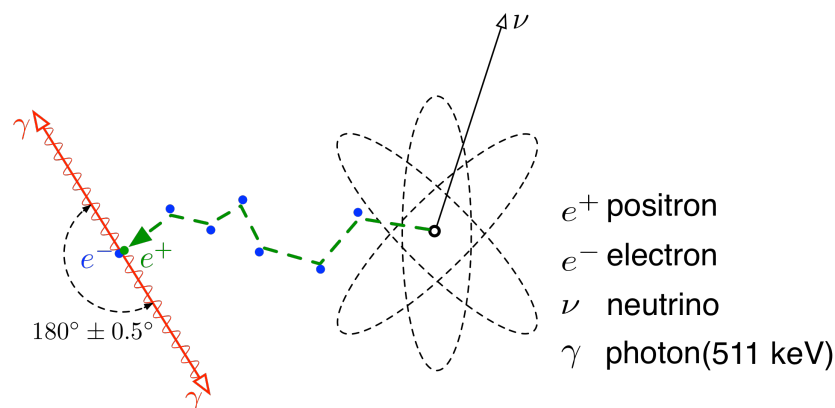
Figure 1.1. Positron-electron annihilation example. The radiotracer undergoes β^+ decay and emits a positron and a neutrino (not detected). Positron loses its kinetic energy and finally annihilates with the electron from patients body. Figure was adapted from [1].

Photons emitted from patients body are registered by detectors and Line-Of-Response (LOR) along which the annihilation happened is reconstructed. Finally, the set of LORs are processed by the image reconstruction algorithm to recover the radiotracer distribution in the patients body.

PET image reconstruction has experienced tremendous improvements over the past 60 plus years since it was first proposed for medical imaging. Spatial resolution has been improved by a factor of 10 and sensitivity by a factor of 40 compared to first PET scanners [8]. Today, total-body PET scanners are being constructed. Two of such projects are: the 2-meter-long EXPLORER scanner that has been recently mounted [9, 10] and the Jagiellonian PET (J-PET) which aims at construction of the modular, cost-effective total-body Time-Of-Flight Position Emission Tomograph based on polymer scintillators [**?**].

The main purpose of this thesis is to develop and implement analytic image reconstruction algorithms: Filtered Back-Projection (FBP), Kernel Density Estima-

tion (KDE) and Time-Of-Flight Filtered Back-Projection (TOF-FBP) in the frame of the J-PET analysis software package (JPetFramework) [11]. This work is a continuation of my bachelor thesis [12].

This thesis is divided into 7 chapters. First chapter contains basic information about PET technique and PET scanners. Second chapter presents the J-PET project. Chapter 3 introduces mathematical background and information about PET reconstruction algorithms. The fourth chapter is dedicated to implementation details in the frame of JPetFramework. Chapter 5 compares reconstruction results. Chapter 6 presents some additional work done as a part of the J-PET framework development team. The thesis finishes with the summary and discussion of possible improvements.

2. J-PET Project

J-PET project is aiming to construct an innovative whole-body Time-Of-Flight-PET (TOF-PET) scanner [13–16]. It was started in 2012 at the Jagiellonian University, Cracow. The J-PET project team consists of a multidisciplinary group that includes physicists, chemists and computer scientists. The project is led by Professor Pawel Moskal.

The crucial idea behind the J-PET scanner is the usage of polymer scintillators instead of the conventional non-organic crystals for the detection of photons emitted from the patients body. Polymer scintillators are much cheaper than crystal scintillators that are currently commercially used and they can be produced in larger blocks that allows to cover larger part of patients body in a single scan. J-PET Data Acquisition System (DAQ) is based on trigger-less Field Programmable Gate Array (FPGA) boards to gather and pre-process registered signals. Plastic scintillators allows to register time with great resolution. The J-PET group is mounting the next highly modular, compact and fully digital prototype with the Silicon Photomultiplier readout, that will further improve the time resolution (see Figure 2.1 right panel). More details about the various ongoing research topics can be found at [17].
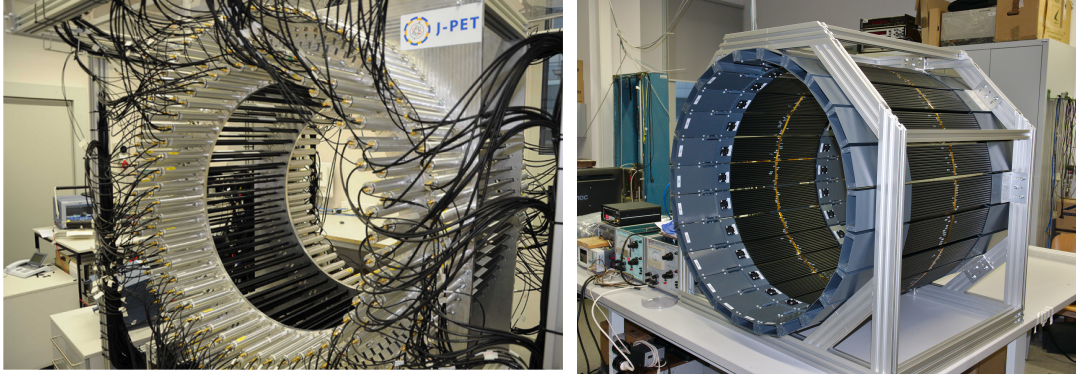
Figure 2.1. On the left: 3 layer J-PET scanner prototype with total of 192 scintillators. On the right: Currently installed modular J-PET scanner prototype. It consists of a single layer with 24 modules with readout from both sides by Silicon Photomultipliers (SiPMs). Each module have 13 scintillators with total of 312 scintillators. It can be inserted into old prototype to create 4 layers scanner.

3. PET Image reconstruction methods

3.1. Basics

3.1.1. Notation and image reconstruction types

The aim of PET image reconstruction algorithms is to obtain the distribution of the radiotracer (image) based on the registered pairs of photons emitted from the patient's body. More precisely, we will denote as $f(x, y)$ the original distribution of the radiotracer [1]. The collected data, are projections of the function $f(x, y)$ that form LORs and are denoted as $p(s, \phi)$ [2] (See Fig 3.1, 3.2). The function $p(s, \phi)$ defines the sinogram, which is a representation of all detected LORs, organized as a set of projections for all possible angles, where a single projection $p(s, \phi^0)$ (or equivalently a row of the sinogram) is formed by integrating along the LOR for all s at a fixed angle ϕ^0 [2]. The relation between p, and f can be expressed in the matrix notation as:

$$\mathbf{p} = \mathbf{Hf} + \mathbf{n} \tag{3.1}$$

Where:

- H: is the image matrix (system matrix),

- p and f: are the vectorized versions of functions $f(x, y)$, $p(s, \phi)$,

- n: represents the vector of observation errors.

---

[1]We will assume the 2-D image case for the simplicity, but the same ideas can be easily extended to the 3-D case.
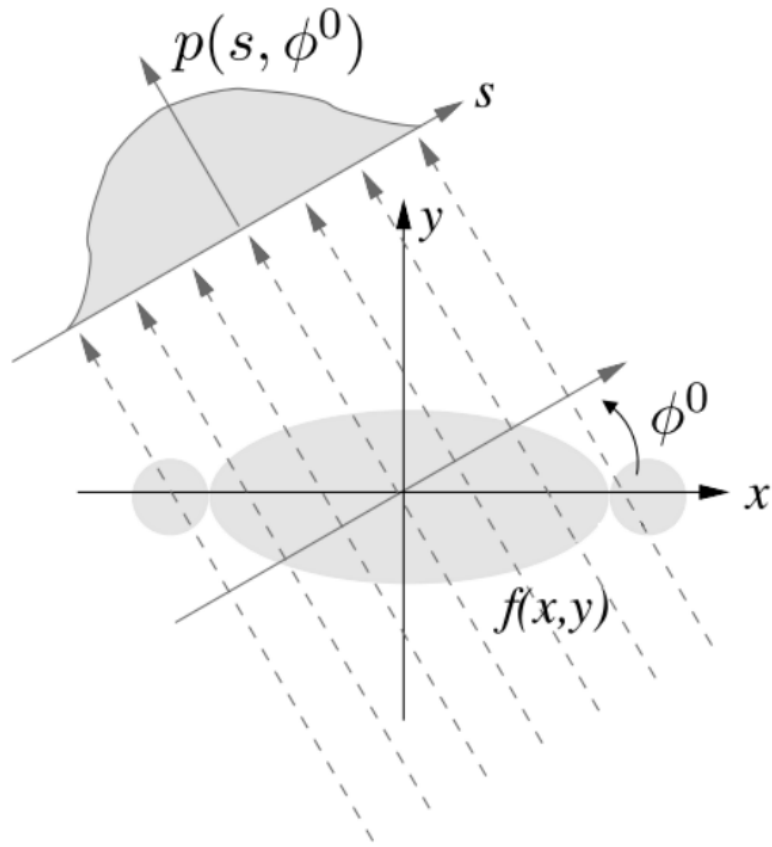
Figure 3.1. Mapping of $f(x, y)$ function to $p(s, \phi)$. The figure is adapted from [2]
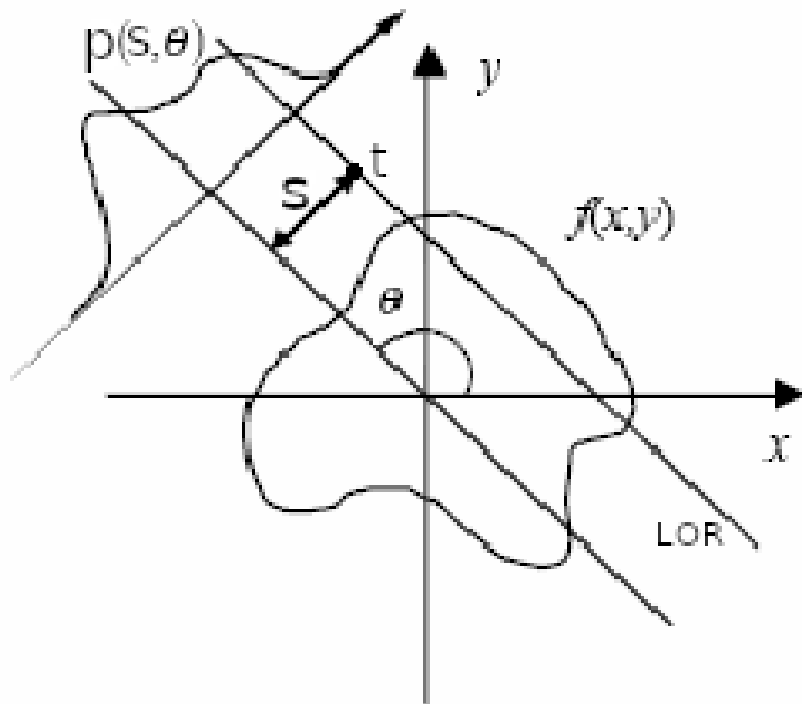
Figure 3.2. FBP notation used in this thesis.

The aim of the reconstruction is to find the estimate of the original f function from the measured set p. Formally, the solution can be obtained from 3.1, by inverting the matrix H.

$$\widehat{\mathbf{f}} = \mathbf{H^{-1}p} \tag{3.2}$$

However due to the stochastic nature of the measurement error, the inversion problem is ill-defined, and some additional conditions must be applied in the reconstruction process.

We can define two general families of algorithms based on different assumptions that are used in the PET tomography. First type is the so-called analytic (or direct) approach which aims to find direct analytic solution from the collected set p, by solving the inverse problem. This approach is based on the assumption that stochastic nature of the measurement error is negligible. In consequence this assumption can lower reconstructed image resolution and have poor noise properties. Most common analytic algorithm is Filtered Back Projection [18–20].

Another way is to use stochastic (iterative) algorithm. It is more accurate description of the actual PET physics and data acquisition. Most of the today iterative algorithms are derived from Maximum Likelihood Estimation Method (MLEM). In MLEM algorithm in each iteration estimation of the reconstructed image is calculated and compared with measured projections [21]. To get satisfactorily results it may be required to calculate many iterations. Iterative reconstruction algorithms are using more accurate mathematical description, but these improvements come at the cost of reconstruction time. Those methods do not provide direct solutions, but instead successively improve (iterate) to estimate better result. [20]

3.1.2. Radon Transform

The Radon Transform $p(s, \phi)$ is defined as an integral of function $f(x, y)$ along the line defined in the (s, ϕ) coordinate system - see Fig. 3.1 [12, 22, 23]:

$$p(s, \phi) = \int_{-\infty}^{\infty} f(x, \phi x + s) dx \tag{3.3}$$

In the PET tomography context, The Radon transform in the 2-D case is the operator that maps the image function f(x,y) into the sinogram $p(s, \phi)$ in projection space. The Inverse Radon Transform can be used to solve analytically the inverse problem, problem of unfolding internal structure of an object by observations of its line integrals. It is corresponding to the back-projection (BP), which transforms data from projection space (s, ϕ) to image space (x, y) [20]:

$$f(x, y) = \int_{0}^{\pi} p(x \cos \phi + y \sin \phi, \phi) d\phi \tag{3.4}$$

3.2. Filtered Back-Projection

FBP is one of the most known analytic algorithm used in the medical tomography e.g. PET and CT [24]. The FBP is in principle used for 2D image reconstruction, however there are several generalizations to 3D.

$$\widehat{p} = \int_{-\infty}^{\infty} |\widehat{s}|(\int_{-\infty}^{\infty} p(\widehat{s},\phi)e^{-j2\pi\widehat{s}v}d\widehat{s})e^{j2\pi sv}ds \qquad (3.5)$$

$$\widehat{f}(x,y) = \int_{0}^{\pi} \widehat{p}(x\cos\phi + y\sin\phi, \phi)d\phi \qquad (3.6)$$

The Filtered Back-Projection is typically written in 2 parts. First is a filtration step that consists of filtration in Fourier space (eq. 3.5). In this part each of the angles in sinogram are transformed to Fourier space and filtered using high pass filter. In this equation a ramp filter $|\widehat{s}|$ was used. After filtration Inverse Fourier Transform is used to get filtered sinogram $\widehat{p}(s,\phi)$. Second step corresponds to application of the discretized version of the Inverse Radon Transform. (eq. 3.6).
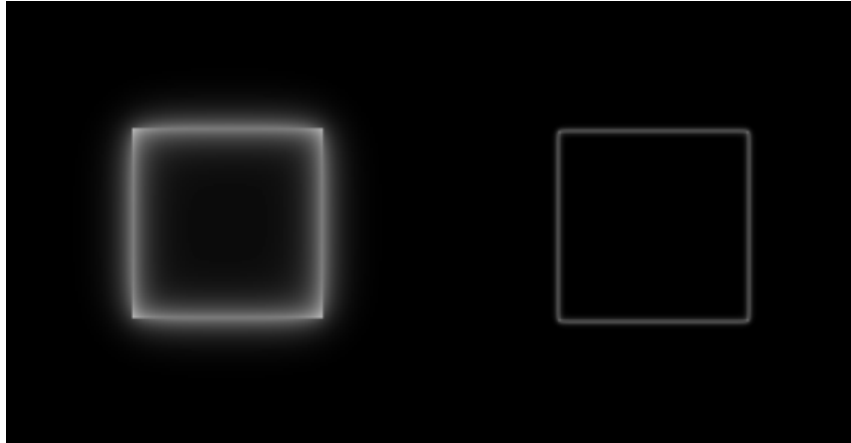
Figure 3.3. Example of influence of high pass filter on the blurred image. On the left: image before filtration. On the right: image after filtration.

3.3. Time-of-flight Filtered Back-Projection

TOF-FBP method allows the information about the time of flight - defined as a difference of registration time of incoming photons - to be incorporat into the reconstruction procedure to improve the quality of reconstructed image. TOF value is related to the shift from the center along the LOR:

$$d = \frac{c\Delta T}{2} \qquad (3.7)$$

where c is the speed of light and ΔT is the time difference of photons registration. The experimental uncertainty of the TOF measurement is included as the parameter of the model describing the probability density of annihilation point localization

along the LOR (TOF kernel). Typically, Gaussian kernel is used, with standard deviation σ corresponding to expected TOF resolution. In the process of back-projection,
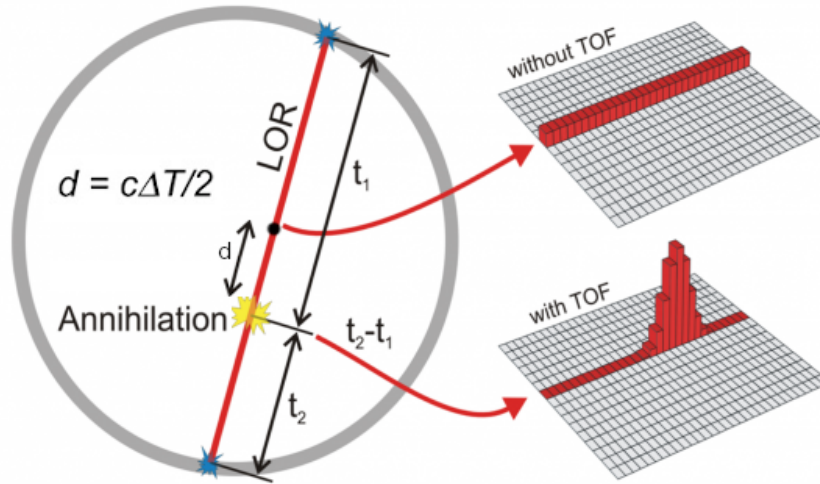
Figure 3.4. Localization of the annihilation point using registered hits times t_1 and t_2 and calculation of displacement from LOR center. Picture was adapted from [3].

each projection is weighted with confidence weighting of TOF bin. The image $f(x, y)$ is reconstructed as follows [25, 26] [3.6]:

$$f(x, y) = \int_0^\pi d\phi \sum_{k=1}^{nTOF} F^{-1}[\widehat{P}_{(\phi,k)}(\rho)W(\rho)](s)e^{\frac{-(t-t_k)^2}{2\sigma^2}} \tag{3.8}$$

Where:

- (s, t): are rotated(with (0, 0) at the center of the LOR) coordinates,

- ϕ: is a projection(LOR) angle,

- ρ: is frequency space coordinate,

- k: is a TOF bin index,

- t_k: position of the center of gaussian distribution in TOF bin k along direction t (See 3.5).

The recent overview of TOF-PET techniques can be found in [27].

3.4. Kernel Density Estimation

The Kernel Density Estimation (KDE) is a nonparametric function to estimate the probability density function of a random variable [28, 29]. Being a part of nonparametric group functions means, it is not required to know information about distribution. Parametric functions requires information about distribution of unknown
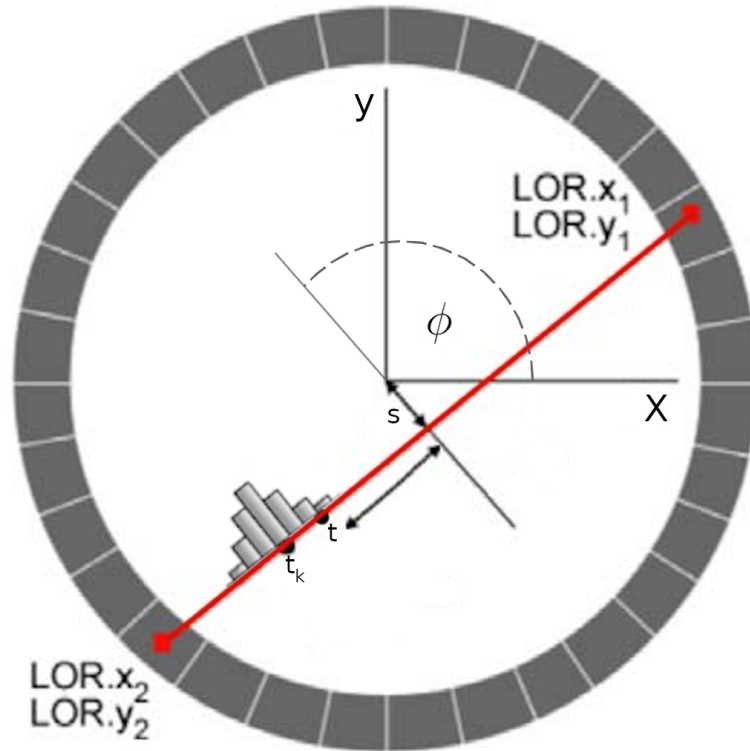
Figure 3.5. Example of single LOR reconstruction using TOF-FBP. After filtration step (not shown) (s,t) is calculated based on (x,y) (from reconstruction image space) and weighted based on distance from center of gaussian distribution t_k. It is done for all TOF bins k.

variable and are only applied to existing values from its (distribution) parameter definitions.

In KDE method instead of filtering sinogram in Fourier space, we iterate through each LOR and weight it using gaussian kernel with standard deviation σ corresponding to saved TOF time for each LOR. As a result we are getting sum of gaussian distribution of each LOR.

4. Implementation in frame of the J-PET framework

4.1. Introduction

This chapter discusses implementation of the reconstruction algorithms in the frame of J-PET framework [11]. All reconstruction algorithms were written in C++ language with C++11 standard in mind. In development, BOOST [30], ROOT [31] and FFTW [32] external frameworks were used. Correctness was ensured by set of unit
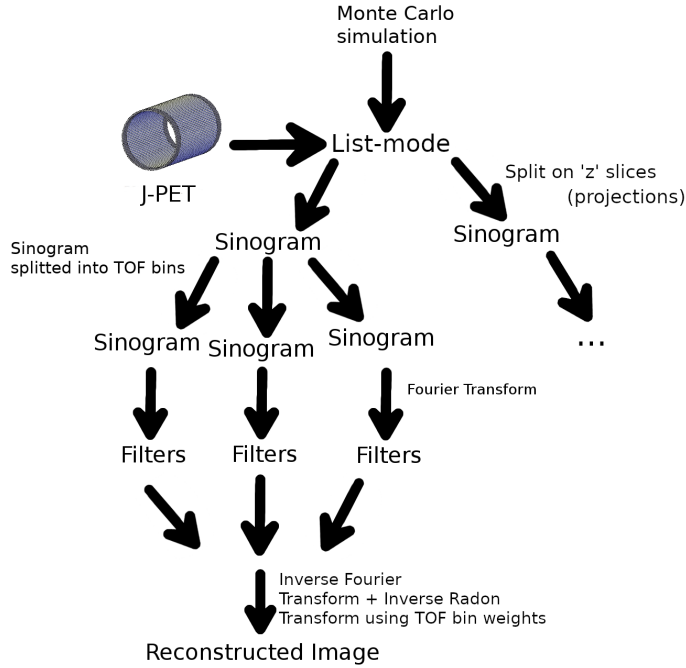
Figure 3.6. Consecutive steps in time-of-flight Filtered Back-Projection (TOF-FBP) algorithm.

tests written using BOOST unit test framework and integration tests using Travis [33] and Jenkins [34]. To isolate the test environment from the host environment Docker [35] was used. The code documentation can be generated with Doxygen [36] package.

The following reconstruction algorithms have been implemented: FBP, TOF-FBP and KDE. As for FBP and TOF-FBP, they are very similar and were implemented in single function. This function allows to pass reference to weighting function that is used to assign weights to each LOR. In the FBP this function always set weights to 1 as LOR has the same contribution along its length. In the TOF-FBP this function calculates appropriate weights based on TOF value. This implementation allows for simple implementation and testing of other kernels for LOR weighting. For the KDE reconstruction there is a dedicated function as it requires additional information about TOF value for each LOR individually.

Similar approach was taken when designing filtration step. Filtration function allows to pass a reference to both FFT function and filter method. This allows for simple change between different implementations and gives the user an ability to apply their own implementations.

Reconstruction starts with JPetManager. JPetManager is a part of JPetFramework and it is responsible for parsing command line arguments as well as of parsing additional parameters given as UserParams in format of json file [37] [2]. Example

---

[2]more information about UserParams is available in [38]
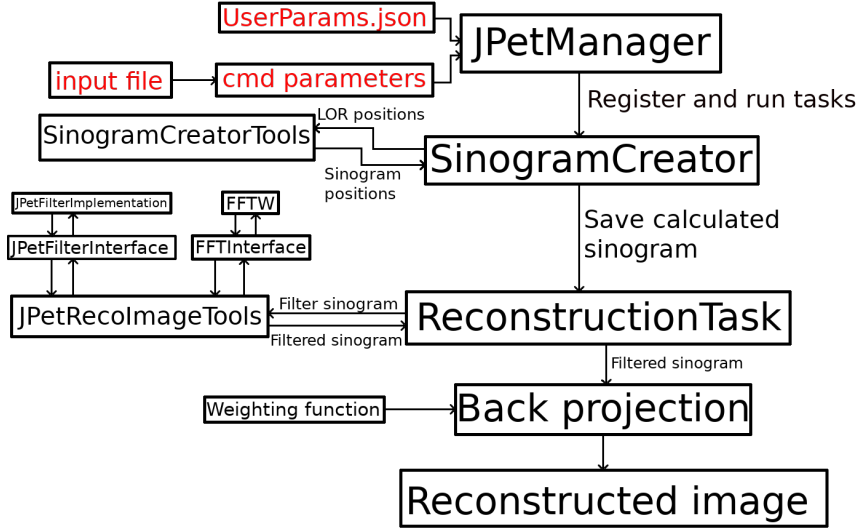
Figure 4.1. Diagram presenting the connection between classes and the reconstruction data flow. The input data was marked with red color.

UserParams file is available in Appendix B. All parameters including choice of the particular algorithms settings and data preprocessing are defined in the configuration file. Beside of that, JPetManager is responsible for registering and running selected external UserTasks, which were not compiled as part of JPetFramework. First task in reconstruction chain, SinogramCreator, is responsible for transforming data from list-mode to sinogram as well as assigning LOR to sinogram slice and applying attenuation correction. As it is most time consuming step in reconstruction, SinogramCreator also allows to save calculated sinogram in ROOT file using ROOT dictionaries. ReconstructionTask as an input takes sinogram and is responsible for filtration and reconstruction. Reconstructed image is saved in Portable Pixel Map format (PPM) [39].

4.2. Data preprocessing

4.2.1. Remapping of oblique LORs to sinogram slices.

In order to include oblique LORs (for which the polar angle $\theta \neq 0$) in reconstruction we need to assign LOR to sinogram slice.

The LOR is represented by the end points $P_1(x_1, y_1, z_1), P_2(x_2, y_2, z_2)$ and the registered times t_1, t_2.

To choose the slice number we calculate approximate position of annihilation point, which lies on the LOR:

$$\theta, \phi, r = cart2sph(x_2 - x_1, y_2 - y_1, z_2 - z_1) \tag{4.1}$$

$$TOF = \frac{c * (t_2 - t_1)}{2} \tag{4.2}$$

$$R_0 = \frac{r}{2} - TOF \tag{4.3}$$

$$x, y, z = sph2cart(\theta, \phi, R_0) \tag{4.4}$$

$$Z_{result} = z + z_1 \tag{4.5}$$

Where:

- $cart2sph(x, y, z)$: function transforming Cartesian coordinates to spherical coordinates,

- TOF: time difference

- R_0: calculated annihilation position,

- $sph2cart(\theta, \phi, r)$: function transforming spherical coordinates to Cartesian coordinates,

- Z_{result}: z coordinate.

We can assign the LOR to a sinogram slice based on the Z_{result} value and the slice length.

After the assignment, we need to rescale the TOF value based on ratio between distance after and before LOR remapping.

$$TOF_{corr} = \frac{\sqrt{(x_2 - x_1)^2 + (y_2 - y_1)^2}}{\sqrt{(x_2 - x_1)^2 + (y_2 - y_1)^2 + (z_2 - z_1)^2}} * TOF \tag{4.6}$$

This relation can be easily derived from the Tales theorem (see Figure [4.2]).:

$$z = \frac{p(z + w)}{p + q} \tag{4.7}$$

$$w = \frac{qz}{p} \tag{4.8}$$

$$z - w = \frac{p(z + w)}{p + q} - \frac{qz}{p} = \frac{p(z + w) - qx(p + q)}{p + q} = \frac{z + w}{p + q}(p - q) \tag{4.9}$$
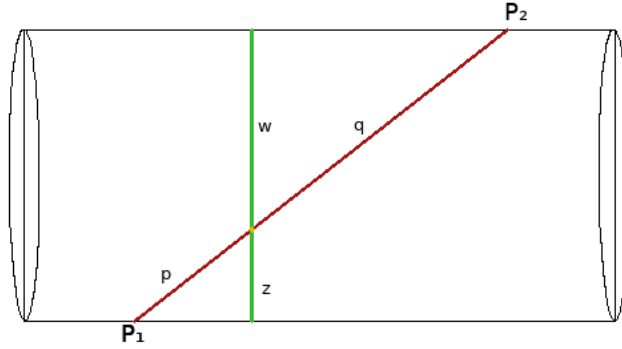
Figure 4.2. Figure shows an example of oblique LOR remapping. The red line denotes original LOR while the green one, the rescaled LOR associated to given sinogram slice. After the procedure the position of the annihilation point is preserved.

4.2.2. Sinograms

To change data from list-mode to projections, we need to transform data from registered LORs (pair of points) to sinogram.

Let $P_1(x_1, y_1)$, $P_2(x_2, y_2)$ be two registered hits. The points P_1, P_2 define a LOR along which annihilation occurred. We want to express the line equation $y = ax + b$ that is passing through P_1 and P_2 in the polar coordinates $l(\rho, \varphi)$:

$$y_1 = ax_1 + b_1 \tag{4.10}$$

$$y_2 = ax_2 + b_1 \tag{4.11}$$

if we subtract 4.11 from 4.10 we get:

$$
a = \begin{cases} 0 & \text{if } x_1 - x_2 = 0 \\ \frac{y_1 - y_2}{x_1 - x_2} & \text{otherwise.} \end{cases}
$$
$$
b = \begin{cases} y_1 & \text{if } x_1 - x_2 = 0 \\ y_1 - \frac{y_1 - y_2}{x_1 - x_2} x_1 & \text{otherwise.} \end{cases}
\tag{4.12}
$$

To calculate ρ we need to know distance between center $(P_3(0,0))$ and intersec-

tion point of line $L(P_1, P_2)$ and perpendicular line passing through $P(0,0)$:

$$
\begin{aligned}
x_i &= \frac{b}{\frac{1}{a} + a} \\
y_i &= -\frac{1}{a} * x_i \\
\rho &= \sqrt{x_i^2 + y_i^2} * sign(y_i)
\end{aligned}
\tag{4.13}
$$

where $sign$ is a function that is equal to 1 if its argument is ≥ 0, and equal to -1 otherwise.

The angle between x-axis and a line passing through $L(P_3, P_i)$ can be expressed as:

$$
\varphi = sign(y_i) * atan2(y_i, x_i) * \left(\frac{180}{\pi}\right)
\tag{4.14}
$$

$atan2$ function has values in the range of: $-\pi < \theta \leq \pi$ but the sinogram is defined only in the range between $[0, \pi]$. We shift values by π based on sign of y_i to get correct range.

4.3. Differences between Filtered Back-Projection and time-of-flight Filtered Back-Projection

From implementation side the only difference between FBP and TOF-FBP is weighting function in the back-projection stage. When FBP is selected, no information about TOF is used, and all weights are set to 1. All bins along the direction of given projection are treated in the same manner. On the other hand, when TOF-FBP is selected, the TOF bins are weighted by the appropriate values based on the measured time of flight information.

```
double JPetRecoImageTools::FBPTOFWeight(double
    lor_tof_center, double lor_position, double sigma)
{
  double x = lor_position - lor_tof_center;
  x *= x;
  double y = 2 * (sigma * sigma);
  return std::exp(-x / y);
}
```

4.4. Storage of data

Processing data in form of list-mode can be very time-consuming. To reduce time required to construct sinogram, a special class was introduced, that allows to serialize sinogram data. Serialization was achieved using ROOT TObject interface.

Beside of that, in both FBP and TOF-FBP most of the sinogram matrix is filled with zeros. In order to reduce amount of memory required by reconstruction algorithms as a base container for data storage for sinogram a sparse matrix was proposed. In order to store information about whole reconstruction data: TOF bin and sinogram slice (on z axis) additional containers are required.

```
using SparseMatrix = boost::numeric::ublas::
    mapped_matrix<double>;
using Matrix3D = std::unordered_map<int, SparseMatrix>;
using WholeSinogram = std::vector<Matrix3D>;
```

Complexity of storage data variables		
variable type	Average case	Worst case
std::unordered_map	O(1)	O(size())
ublas::mapped_matrix	O(log(size()))	O(log(size()))

4.5. Attenuation correction

A number of factors can lower reconstructed image quality. One of them is the photon attenuation due to the secondary interactions in the phantom. Attenuation correction methods requires finding an attenuation map. After the generation of attenuation map it can be incorporated into reconstruction algorithm to correct for this effect.
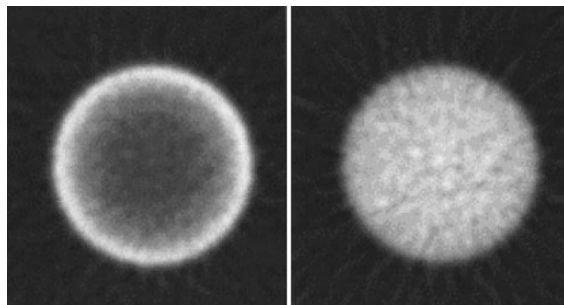
Figure 4.3. Example of influence of attenuation correction on uniform cylindric phantom. On the left: reconstruction without attenuation correction. On the right: reconstruction with attenuation correction. Loss of activity in the center of phantom is recovered after applying attenuation correction. Figure was adapted from [4]

Generated attenuation map corresponds to probability of photon attenuation. To correct data using this map, random generator that produces uniform distribution is required. After generating a random value for each registered LOR one compares its to values from attenuation map. If calculated value is greater or equal to random value, you remove this particular LOR from reconstruction.

In this thesis, attenuation map was generated basing on the information about probability of absorption of point (x, y, z) in the GATE simulation. This approach has a disadvantage of not including information about direction of LOR in probability. LORs that annihilate in the same point, but have different direction can have different probability of absorption. This simplification can cause errors in reconstruction, especially on the edges of the phantom (as difference between calculated attenuation value and real one is the largest for points on the edge of phantom). Attenuation map was generated by L. Raczynski and more information can be found (in unpublished article) [40].

5. Results

Several input data samples have been used during the implementation and evaluation phases:

- MC Point source with back-to-back two-photon emissions in the middle and same one moved 4 cm from the center on the x-axis - ideal tomograph - 100M LORs for each source

- MC Simulated data of 6 points with back-to-back two-photon emissions in J-PET tomograph and same data obtained by J-PET tomograph (more information in Appendix C) - 3 layer J-PET tomograph - MC: 325000 LORs, obtained data: 260513 LORs

- MC Simulated data of NEMA phantom in J-PET tomograph (more information available at Appendix A) - ideal tomograph - 50M LORs

Description of ideal J-PET tomograph is available in Appendix E. Data aquisited by J-PET tomograph was prefiltered according to the conditions described in Appendix C. As for reconstruction options, all phantoms were reconstructed using the same options. For image size 4mm pixels was used with 2cm z slices. For TOF-FBP 50 ps bin size was set along with 600 ps sigma for TOF.

As a first and the most simple point-line phantom was used. 10^6 LORs of phantom were simulated with $\sigma_{TOF} = 400ps$. Reconstruction produced very similar results for both FBP and TOF-FBP and showed that reconstruction algorithms indeed reconstruct the expected phantom. In both reconstructions, Hann filter without cut-off were used (equations corresponding to all the filters used can be found in Appendix D). The cut-off parameter was defined in such a way, that without cut-off (cut-off parameter equals 1) means no additional (other than filter already have) changes in the frequency space are done. The reconstructed images are shown in Figures 5.1 and 5.2.

Figure 5.1. Comparision between FBP and TOF-FBP reconstruction of Monte-Carlo generated point-like phantom in the geometrical center of the tomograph.
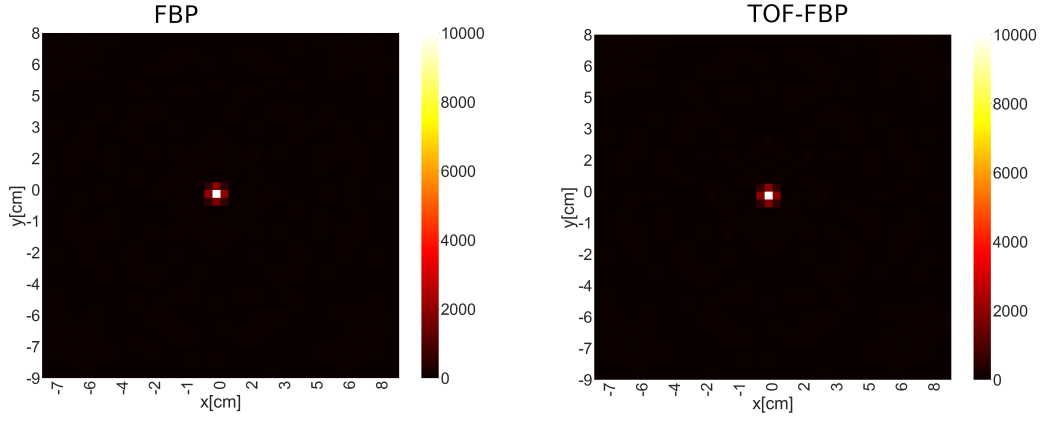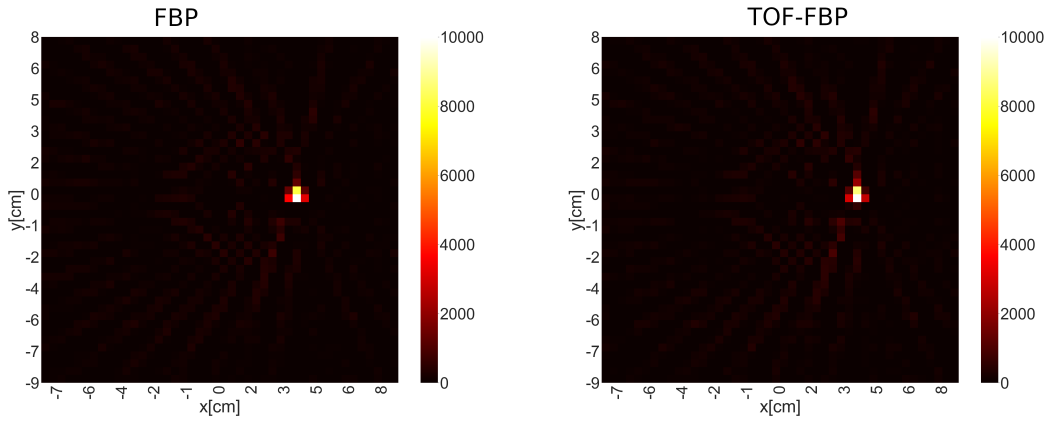

Figure 5.2. Comparision between FBP and TOF-FBP reconstruction of Monte-Carlo generated point-like phantom moved 4 cm from the center of the tomograph.
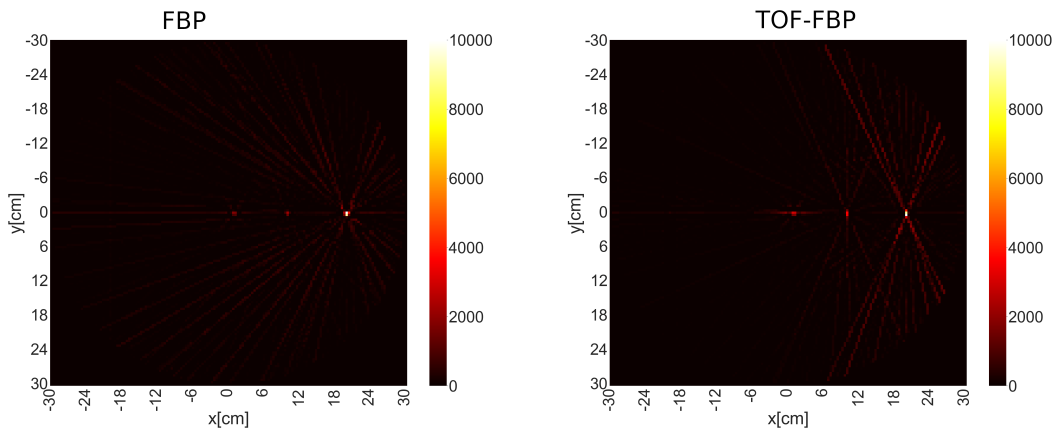

Figure 5.3. Comparison between FBP (left side) and TOF-FBP (right side) of $z = 0$ sinogram slice for the MC simulations of 6 sources.

Figure 5.4. Comparison between FBP (left side) and TOF-FBP (right side) of $z = -18.75$ sinogram slice for the MC simulations of 6 sources.

Next comparison was done using both simulated 3 layer J-PET tomograph and data obtained by 3 layer J-PET tomograph prototype. 325000 simulated LORs were generated with $\sigma_{TOF} = 500ps$. For data acquired by the tomograph, six sources with different activities were placed a the single plane (according to description in Appendix C). For J-PET data reconstruction, 20 files were used with a total of 260513 LORs after filtering. Results of the reconstruction can be found in Figures 5.3, 5.4 for simulation and Figures 5.5, 5.6 from tomograph data. There are visible differences between FBP and TOF-FBP reconstructions.

Figure 5.5. Comparison between FBP(left side) and TOF-FBP(right side) of $z = 0$ sinogram slice of 6 sources phantom registered by J-PET tomograph.

The next set of tests have been performed with the NEMA phantoms simulated by the GATE package. Figures 5.9 and 5.10 show reconstruction of NEMA phantom using both FBP and TOF-FBP with different filters. For each set of reconstructions, CRC and BV values were calculated according to Appendix A. Results are presented in Table 5.1 for FBP and in Table 5.2 for TOF-FBP.

26

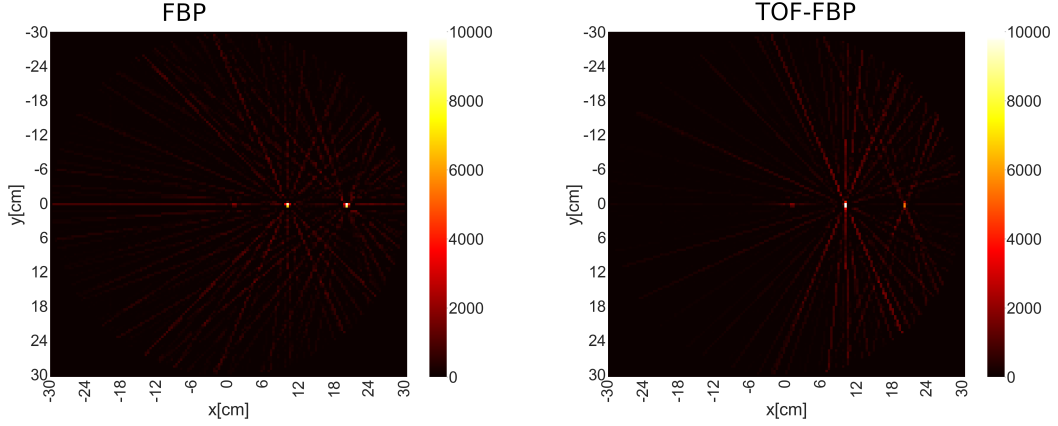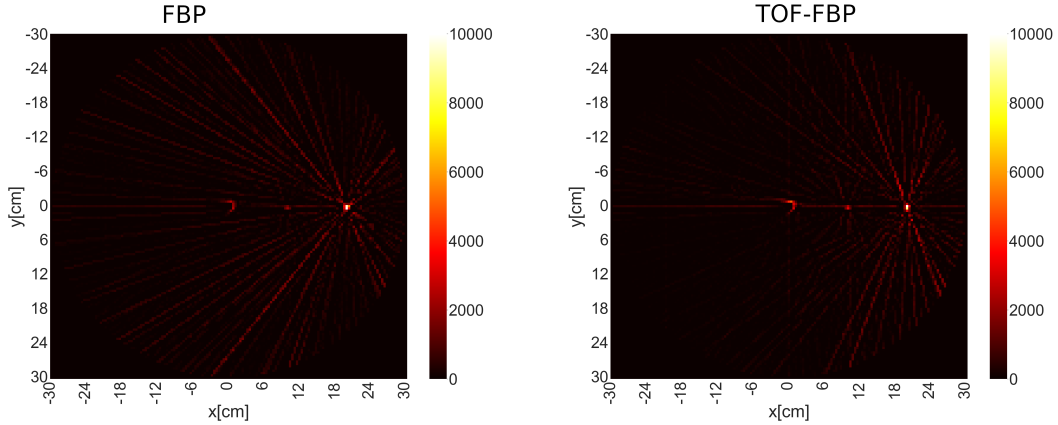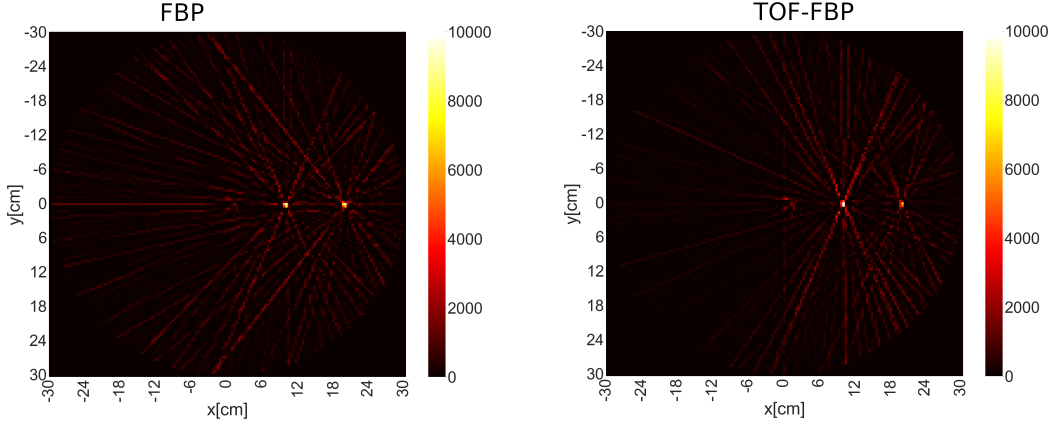**Figure 5.6.** Comparison between FBP(left side) and TOF-FBP(right side) of $z = -18.75$ sinogram slice of 6 sources phantom registered by J-PET tomograph.

Filter	sphere22mm		sphere17mm		sphere13mm		sphere10mm	
	BV	CRC	BV	CRC	BV	CRC	BV	CRC
RamLak	0.23	.028	0.23	.018	0.24	0.07	0.23	0.09
SheppLogan	0.14	0.75	0.20	0.66	0.21	0.50	0.30	0.70
Ridgelet	0.31	1.00	0.31	0.88	0.32	0.54	0.40	0.66
Hann	0.10	0.76	0.15	0.79	0.19	0.58	0.26	0.84
Hamming	0.10	0.64	0.14	0.63	0.16	0.45	0.22	0.65

Table 5.1. CRC/BV values for each of ROIs for FBP reconstruction.

Filter	sphere22mm		sphere17mm		sphere13mm		sphere10mm	
	BV	CRC	BV	CRC	BV	CRC	BV	CRC
RamLak	0.53	0.50	0.53	0.39	0.53	0.09	0.51	0.10
SheppLogan	0.20	1.10	0.23	1.04	0.24	0.73	0.33	0.91
Ridgelet	0.31	1.01	0.31	0.88	0.32	0.54	0.34	0.66
Hann	0.15	1.07	0.18	1.15	0.23	0.80	0.30	1.05
Hamming	0.17	0.96	0.18	1.00	0.20	0.66	0.24	0.86

Table 5.2. CRC/BV values for each of ROIs for TOF-FBP reconstruction.

Figures 5.7 shows BV, CRC values for different filter cutoff values. For FBP SheppLogan filter was selected and for TOF-FBP Hamming filter was selected. Additionally to that, parameter Q was calculated as the absolute distance to ideal reconstruction (BV = 0, CRC = 1):

$$Q = |1 - CRC| + BV \tag{5.1}$$

27
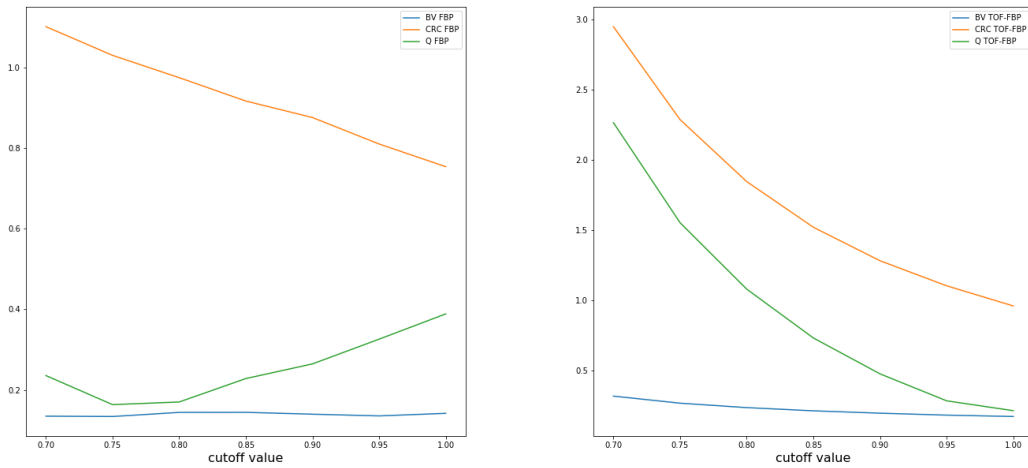
Figure 5.7. BV, CRC and Q values of FBP reconstruction with SheppLogan filter (left) and TOF-FBP reconstruction with Hamming filter (right) using different cutoff values.
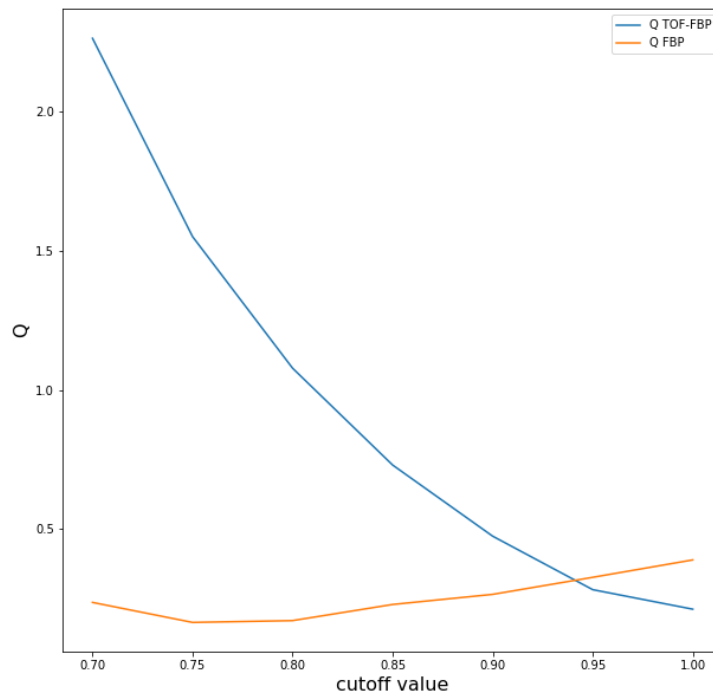
Figure 5.8. Q value for FBP and TOF-FBP reconstruction algorithms.

6. Other activities

As a part of J-PET framework core development team I was responsible for designing and introducing of the Continuous Integration (CI) system based on Jenkins and
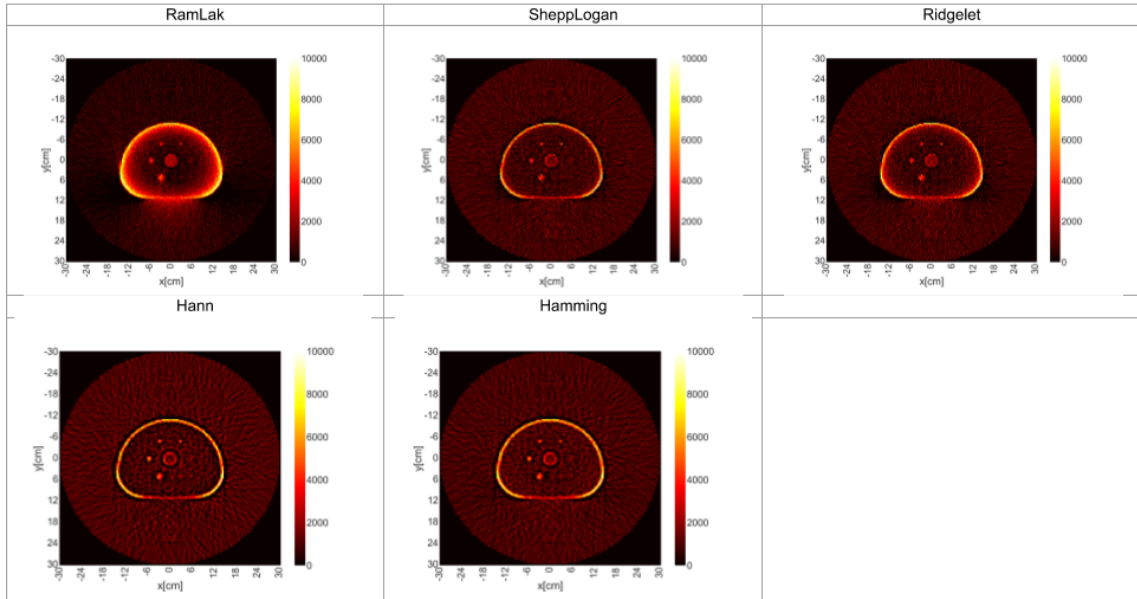
Figure 5.9. Reconstruction of simulated NEMA phantom in J-PET tomograph using FBP with different filters.
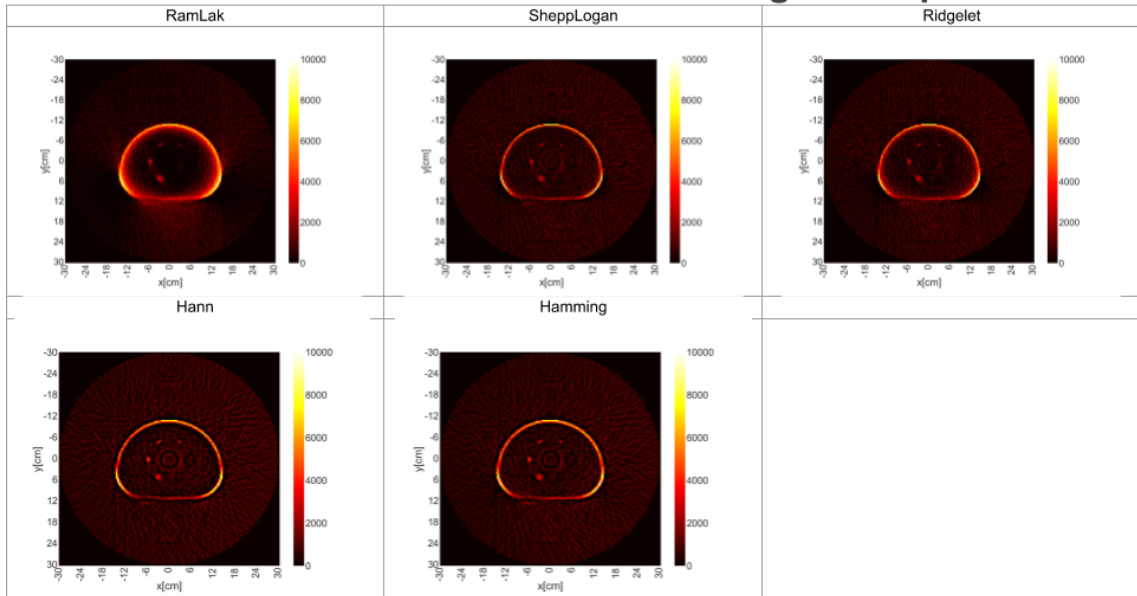
Figure 5.10. Reconstruction of simulated NEMA phantom in J-PET tomograph using TOF-FBP with different filters.

Docker. Beside of already used CI system (Travis) it allowed to take more control over testing environment as it was running tests in an isolated environment using Docker. Jenkins with its plugins also allows to generate automatic static analysis raports as well as test coverage raports.

Another task which I was responsible for, was the adaptation of CMake system to more modern way. In the process whole cmake files was rewritten with modern cmake

29

style to match current standards. During my whole work I participated actively in the bug fixing and the code maintenance process.

7. Summary

The main objective of this thesis was the implementation of analytic reconstruction algorithms in the frame of J-PET framework software. It was achieved using C++ language. Implemented reconstruction algorithms have been tested using several phantoms generated with Monte Carlo simulations, as well as with data gathered by the the 3-layer prototype of J-PET tomograph.

Presented results indicate that implemented reconstruction algorithms provide expected reconstruction image. There is a difference between FBP and TOF-FBP results (especially seen in six sources phantom), but still more corrections needs to be implemented (e.g. geometrical acceptance of tomograph). Implemented solution gives comparable result to other well known implementations of FBP and TOF-FBP (e.g. STIR). In reconstruction of the NEMA phantom, the best results have been obtained using the Shepp-Logan filter with the cut-off parametr equal to 0.75 of Nyquist frequency (corresponding to the Background Variability of 0.13 and the Contrast Recovery Coefficient equal to 1.03 for high activity region of radius 22 mm). For the Time-of-Fligth Filtered Back-Projection algorithm, the best reconstruction was obtained using the Hamming filter with the cut-off parameter equal to Nyquist frequency (corresponding to the Background Variability of 0.17 and the Contrast Recovery Coefficient equal to 0.96 for high activity region of radius 22 mm).

There are still room for further studies and improvements. More tests are needed for better understanding influence of cut-off parameter in filters as well as sinogram TOF bin size. Next step will consist of the implementation of 3D version of the FBP algorithm.

References

[1] Jens Maus. *Event-Driven Motion Compensation in Positron Emission Tomography: Development of a Clinically Applicable Method.* PhD thesis, 11 2008.

[2] L Raczyński, Wojciech Wiślicki, K Klimaszewski, Wojciech Krzemien, Paweł Kowalski, R Shopa, Piotr Bialas, C Curceanu, Eryk Czerwiński, K Dulski, A Gajos, Bartosz Głowacz, M Gorgol, B Hiesmayr, Jasinska Bozena, D Kisielewska-Kamińska, Grzegorz Korcyl, Tomasz Kozik, Nikodem Krawczyk, and Pawel Moskal. Introduction of total variation regularization into filtered backprojection algorithm. *Acta Physica Polonica B*, 48, 10 2017. doi: 10.5506/APhysPolB.48.1611.

[3] The 10ps challange website. https://the10ps-challenge.org. Accessed: 2019-08-01.

[4] Habib Zaidi and Bruce Hasegawa. Determination of the attenuation map in emission tomography. *Journal of Nuclear Medicine*, 44(2):291–315, 2003. URL http://jnm.snmjournals.org/content/44/2/291.abstract.

[5] M. Pawlik-Niedzwiecka, S. Niedzwiecki, D. Alfs, P. Bialas, C. Curceanu, E. Czerwinski, K. Dulski, A. Gajos, B. Glowacz, M. Gorgol, B. C. Hiesmayr, B. Jasinska, D. Kisielewska, G. Korcyl, P. Kowalski, T. Kozik, N. Krawczyk, W. Krzemien, E. Kubicz, M. Mohammed, M. Palka, L. Raczynski, J. Raj, Z. Rudy, Shivani, M. Silarski, M. Skurzok, N. G. Sharma, S. Sharma, R. Y. Shopa, A. Strzelecki, A. Wieczorek, W. Wislicki, B. Zgardzinska, M. Zielinski, and P. Moskal. Preliminary studies of j-pet detector spatial resolution. *Acta Physica Polonica. Series A: General Physics, Physics of Condensed Matter, Optics and Quantum Electronics, Atomic and Molecular Physics, Applied Physics*, 132(5):1645–1648, 11 2017. ISSN 0587-4246. doi: 10.12693/APhysPolA.132.1645.

[6] Leah H. Portnow, David E. Vaillancourt, and Michael S. Okun. The history of cerebral pet scanning. *Neurology*, 80(10):952–956, 2013. ISSN 0028-3878. doi: 10.1212/WNL.0b013e318285c135. URL https://n.neurology.org/content/80/10/952.

[7] Dayton A. Rich. A brief history of positron emission tomography. *Journal of Nuclear Medicine Technology*, 25(1):4–11, 1997.

[8] David W. Townsend Terry Jones. History and future technical innovation in positron emission tomography. *Journal of Medical Imaging*, 4(1):1 – 17 – 17, 2017. doi: 10.1117/1.JMI.4.1.011013. URL https://doi.org/10.1117/1.JMI.4.1.011013.

[9] Simon R. Cherry, Ramsey D. Badawi, Joel S. Karp, William W. Moses, Pat Price, and Terry Jones. Total-body imaging: Transforming the role of positron emission tomography. *Science Translational Medicine*, 9(381), 2017. ISSN 1946-6234. doi: 10.1126/scitranslmed.aaf6169. URL https://stm.sciencemag.org/content/9/381/eaaf6169.

[10] Ramsey D. Badawi, Hongcheng Shi, Pengcheng Hu, Shuguang Chen, Tianyi Xu, Patricia M. Price, Yu Ding, Benjamin A. Spencer, Lorenzo Nardo, Weiping Liu, Jun Bao, Terry Jones, Hongdi Li, and Simon R. Cherry. First human imaging studies with the explorer total-body pet scanner. *Journal of Nuclear Medicine*, 60(3):299–303, 2019. doi: 10.2967/jnumed.119.226498. URL http://jnm.snmjournals.org/content/60/3/299.abstract.

[11] Wojciech Krzemien, A Gajos, A Gruntowski, K Stola, Damian Trybek, T Bednarski, Piotr Bialas, Eryk Czerwinski, D Kaminska, L Kaplon, A Kochanowski, Grzegorz Korcyl, J Kowal, Pawel, Kowalski, Tomasz Kozik, Ewelina Kubicz, Pawel Moskal, Szymon Niedzwiecki, M Palka, and Natalia Zon. Analysis framework for the j-pet scanner. *Acta Physica Polonica A*, 127, 03 2015. doi: 10.12693/APhysPolA.127.1491.

[12] Kamil Rakoczy. Development of the event display and the adaptation of various image reconstruction algorithms for the j-pet tomography scanner. Bachelor's thesis, Uniwersytet Jagiellonski, 2017.

[13] Pawel Moskal. Strip device and the method for the determination of the place and response time of the gamma quanta and the application of the device for the positron emission thomography, 2010.

[14] Pawel Moskal. Matrix device and the method for the determination of the place and response time of the gamma quanta and the application of the device for the positron emission thomography, 2011.

[15] P. Moskal, P. Salabura, M. Silarski, J. Smyrski, J. Zdebik, and M. Zielinski. Novel detector systems for the Positron Emission Tomography. *Bio-Algorithms Med-Syst.*, 7(2):73, 2011.

[16] P. Moskal et al. A novel method for the line-of-response and time-of-flight reconstruction in TOF-PET detectors based on a library of synchronized model signals. *Nucl. Instrum. Meth.*, A775:54–62, 2015. doi: 10.1016/j.nima.2014.12.005.

[17] J-PET website. http://koza.if.uj.edu.pl/pet/. Accessed: 2019-08-01.

[18] L Raczyński, Wojciech Wiślicki, K Klimaszewski, Wojciech Krzemien, Paweł Kowalski, R Shopa, Piotr Bialas, C Curceanu, Eryk Czerwiński, K Dulski, A Gajos, Bartosz Głowacz, M Gorgol, B Hiesmayr, Jasinska Bozena, D Kisielewska-Kamińska, Grzegorz Korcyl, Tomasz Kozik, Nikodem Krawczyk, and Pawel Moskal. Introduction of total variation regularization into filtered backprojection algorithm. *Acta Physica Polonica B*, 48, 10 2017. doi: 10.5506/APhysPolB.48.1611.

[19] Shan Tong, Adam Alessio, and Paul Kinahan. Image reconstruction for pet/ct scanners: Past achievements and future challenges. *Imaging in medicine*, 2: 529–545, 10 2010. doi: 10.2217/iim.10.49.

[20] Adam M. Alessio and Paul E. Kinahan. PET Image Reconstruction. 2005.

[21] G.B. Saha. *Basics of PET Imaging: Physics, Chemistry, and Regulations*. Springer New York, 2010. ISBN 9781441908056. URL https://books.google.pl/books?id=gb6-qYjmL8UC.

[22] S. Helgason. *The Radon Transform*. Progress in Mathematics. Birkhäuser Boston, 1999. ISBN 9780817641092. URL https://books.google.pl/books?id=tq3eStnBwIUC.

[23] Peter Aundal Toft. The radon transform - theory and implementation. 1996.

[24] Michel Defrise, Paul E. Kinahan, and Christian J. Michel. *Image Reconstruction Algorithms in PET*, pages 63–91. Springer London, London, 2005. ISBN 978-1-84628-007-8. doi: 10.1007/1-84628-007-9_4. URL https://doi.org/10.1007/1-84628-007-9_4.

[25] Maurizio Conti, Bernard Bendriem, Mike Casey, Mu Chen, Frank Kehren, Christian Michel, and Vladimir Panin. First experimental results of time-of-flight reconstruction on an LSO PET scanner. *Physics in Medicine and Biology*, 50(19):4507–4526, sep 2005. doi: 10.1088/0031-9155/50/19/006. URL https://doi.org/10.1088%2F0031-9155%2F50%2F19%2F006.

[26] Michel Defrise, Michael E Casey, Christian Michel, and Maurizio Conti. Fourier rebinning of time-of-flight PET data. *Physics in Medicine and Biology*, 50 (12):2749–2763, may 2005. doi: 10.1088/0031-9155/50/12/002. URL https://doi.org/10.1088%2F0031-9155%2F50%2F12%2F002.

[27] Stefaan Vandenberghe, Ekaterina Mikhaylova, Ester D'Hoe, Pieter Mollet, and Joel S. Karp. Recent developments in time-of-flight pet. *EJNMMI Physics*, 3, 12 2016. doi: 10.1186/s40658-016-0138-3.

[28] Yen-Chi Chen. A Tutorial on Kernel Density Estimation and Recent Advances. *arXiv e-prints*, art. arXiv:1704.03924, Apr 2017.

[29] Emanuel Parzen. On estimation of a probability density function and mode. *Ann. Math. Statist.*, 33(3):1065–1076, 09 1962. doi: 10.1214/aoms/1177704472. URL https://doi.org/10.1214/aoms/1177704472.

[30] Boost website. https://www.boost.org. Accessed: 2019-08-01.

[31] ROOT website. https://root.cern.ch. Accessed: 2019-08-01.

[32] FFTW website. http://www.fftw.org. Accessed: 2019-08-01.

[33] Travis CI website. https://travis-ci.com. Accessed: 2019-08-01.

[34] Jenkins website. https://jenkins.io. Accessed: 2019-08-01.

[35] Docker website. https://www.docker.com. Accessed: 2019-08-01.

[36] Doxygen website. http://www.doxygen.nl. Accessed: 2019-08-01.

[37] JSON website. https://www.json.org. Accessed: 2019-08-01.

[38] Klara Muzalewska. Development of the option manager module in the frame of the J-Pet tomography software package. Bachelor's thesis, Uniwersytet Jagiellonski, 2017.

[39] PPM website. http://netpbm.sourceforge.net/doc/ppm.html. Accessed: 2019-08-01.

[40] L. Raczyński et al. 3D TOF-PET Image Reconstruction Using Total Variation Regularization. 2019.

[41] NEMA/IEC. Radionuclide imaging devices - characteristics and test conditions - part 1: Positron emission tomographs. International standard, International Electrotechnical Commission (IEC), Geneva, Switzerland, 1998. URL https://webstore.iec.ch/publication/5712.

[42] G. L. Zeng. Revisit of the ramp filter. In *2014 IEEE Nuclear Science Symposium and Medical Imaging Conference (NSS/MIC)*, pages 1–6, Nov 2014. doi: 10.1109/NSSMIC.2014.7430796.

Appendix

A. Appendix A

The National Electrical Manufacturers Association (NEMA) was funded in 1926 and is the largest trade association of electrical equipment manufacturers in the United States. NEMA-NU-2-2012 presents standards of performance measurements for Positron Emission Tomographs that allows to compare between different tomographs. NEMA IEC Phantom Body was used for image reconstruction quality measurements. The NEMA IEC Phantom consists of six hot spheres and three cold one. The main applications of NEMA IEC Body Phantom are [41]:

- Simulation of whole-body imaging especially using PET and camera-based coincidence imaging techniques

- Evaluation of reconstructed image quality in whole-body PET and camera-based coincidence imaging

- Determination of the coincidence count rate characteristics in brain and cardiac imaging

- Evaluation of the relationship between true coincidence count rate and radioactivity

- Determination of the address errors caused by address pile up

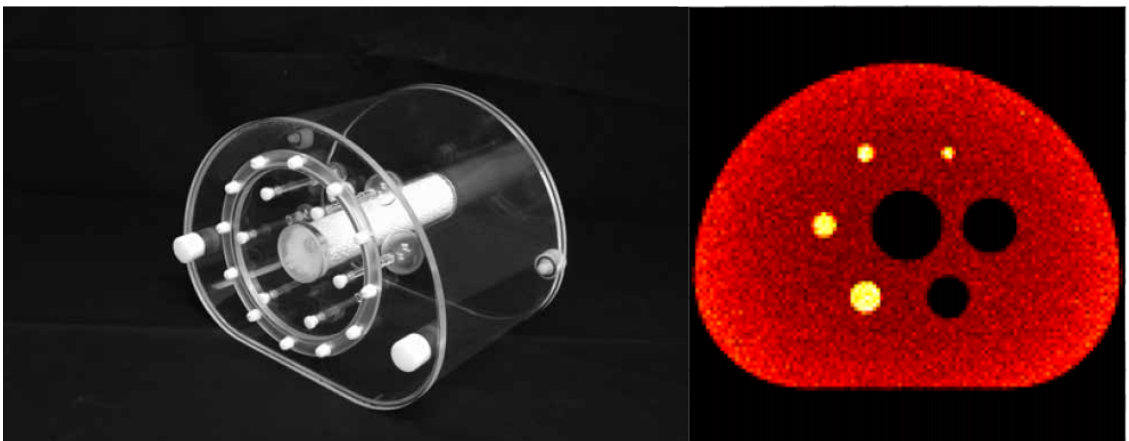- Evaluation of the count loss correction scheme

- Research

Figure A.1. Nema IEC Body Phantom (left side) with example of simulated annihilations (right)

To compare the image reconstruction quality of different reconstruction algorithms we calculate contrast recovery coefficient (CRC) for the largest (22 mm) hot

sphere and background variability (BV) from the reconstructed images:

$$CRC = \frac{\frac{\text{hot mean}}{\text{background mean}} - 1}{\text{true contrast} - 1} \qquad (A.1)$$

The background variability is defined as standard deviation of the values inside background region-of-interest(ROI):

$$BV = \frac{\text{background std}}{\text{background mean}} \qquad (A.2)$$

The BV controls background noise in the reconstructed image. The higher BV is, the more noisy reconstructed is. On the other hand CRC controls contrast between background noise and interested hot ROI, the higher CRC is, there is more contrast between hot ROI and background. To increase reconstructed image quality, we should maximize CRC with in the same time try to minimalize BV.

B. Appendix B

Example UserParams json file:

```
{
    "JPetManager_useTasks_std::vector<std::string>": ["
        SinogramCreator", "reco.unk.evt", "sino", "
        ReconstructionTask", "sino", "reco"],
    "SinogramCreator_OutFileName_std::string": "sinogram.
        root",
    "SinogramCreator_ReconstructionDistanceAccuracy_float
        ": 0.4,
    "SinogramCreator_SinogramZSplitNumber_int": 25,
    "SinogramCreator_EnableObliqueLORRemapping_bool":
        true,
    "ReconstructionTask_ReconstructSliceNumbers_std::
        vector<int>": [],
    "ReconstructionTask_FilterCutOffValueBegin_float":
        0.3,
    "ReconstructionTask_FilterCutOffValueEnd_float": 1.0,
    "ReconstructionTask_FilterCutOffValueStep_float":
        0.5,
    "ReconstructionTask_FilterName_std::string": "Hann",
    "ReconstructionTask_ReconstructionType_std::string":
        "FBP",
    "ReconstructionTask_OutFileName_std::string": "./
        reconstruction/"
```

```
    }
```

C. Appendix C

All ^{22}Na point sources were placed according to NEMA-NU-2-2012 standard [41]. To place sources in same x plane styrofoam panel were prepared. Styrofoam has been chosen, because of its low density $(1.07\frac{g}{cm^3})$ and its low probability of gamma scattering. Additionally experimental data was prefiltered according to following conditions: Prefiltering conditions used for the selection of LOR candidates from the experimental data:

- only 2 hits registered in the event

- $y_{anihhilation} \in [-23cm, 23cm]$

- $z_{anihhilation} \in [-23cm, 23cm]$

- LOR distance from geometrical center of detector $< 25cm$ in x and y plane

- minimum angle between 2 scintillators $> 20°$

- histogram of TOT sum for sideA and sideB, for four thresholds, in range of 15ns to 26ns

More information about source placement and data prefiltration can be found in [5].

D. Appendix D

To reduce noise in reconstructed images, high-pass filter was used. Ramp filter was selected with multiple windowing functions. It is known, that directly sampling of ramp filter introduces error in DC component [42]. To correct this error, DC value was filtered with value 0.02. Before filtering, data was padded with zeros to nearest power of 2 of 2 * length of data.

Ramp filter equation:

$$f(x) = \begin{cases} 0 & \text{if } x > \text{cutoff value} \\ \frac{x}{\text{cutoff}} & \text{otherwise.} \end{cases} \tag{D.1}$$

Hann filter is multiplication of ramp filter with Hann window:
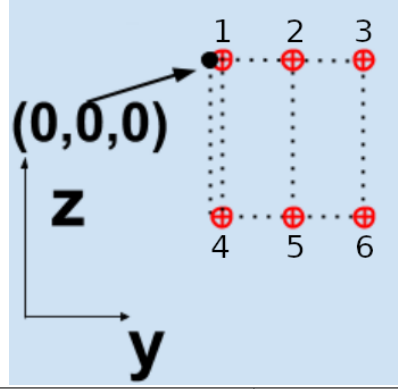
ID	Source position	Source activity
1	$(0, 1, 0)$	204 kBq
2	$(0, 10, 0)$	207 kBq
3	$(0, 20, 0)$	1134 kBq
4	$(0, 1, -18.75)$	1131 kBq
5	$(0, 10, -18.75)$	6198 kBq
6	$(0, 20, -18.75)$	7601 kBq

Figure C.1. Position of sources inside J-PET tomograph. Picture was adapted from [5]

$$f(x) = \begin{cases} 0 & \text{if } x > \text{cutoff value} \\ ramp(x) * sin(\frac{\pi * x}{cutoff})^2 & \text{otherwise.} \end{cases} \tag{D.2}$$

Hamming filter is multiplication of ramp filter with Hamming window:

$$f(x) = \begin{cases} 0 & \text{if } x > \text{cutoff value} \\ ramp(x) * (0.54 - (0.46 * cos(2 * \pi * x))) & \text{otherwise.} \end{cases} \tag{D.3}$$

SheppLogan filter is multiplication of ramp filter with SheppLogan window:

$$f(x) = \begin{cases} 0 & \text{if } x > \text{cutoff value} \\ ramp(x) * sin(\frac{2 * \pi * x}{\pi * \text{cutoff}}) & \text{otherwise.} \end{cases} \tag{D.4}$$

Ridgelet filter is multiplication of ramp filter with Ridgelet window:

$$f(x) = \begin{cases} 0 & \text{if } x > \text{cutoff value} \\ ramp(x) * \sqrt{\frac{x}{\text{cutoff}}} & \text{otherwise.} \end{cases} \tag{D.5}$$
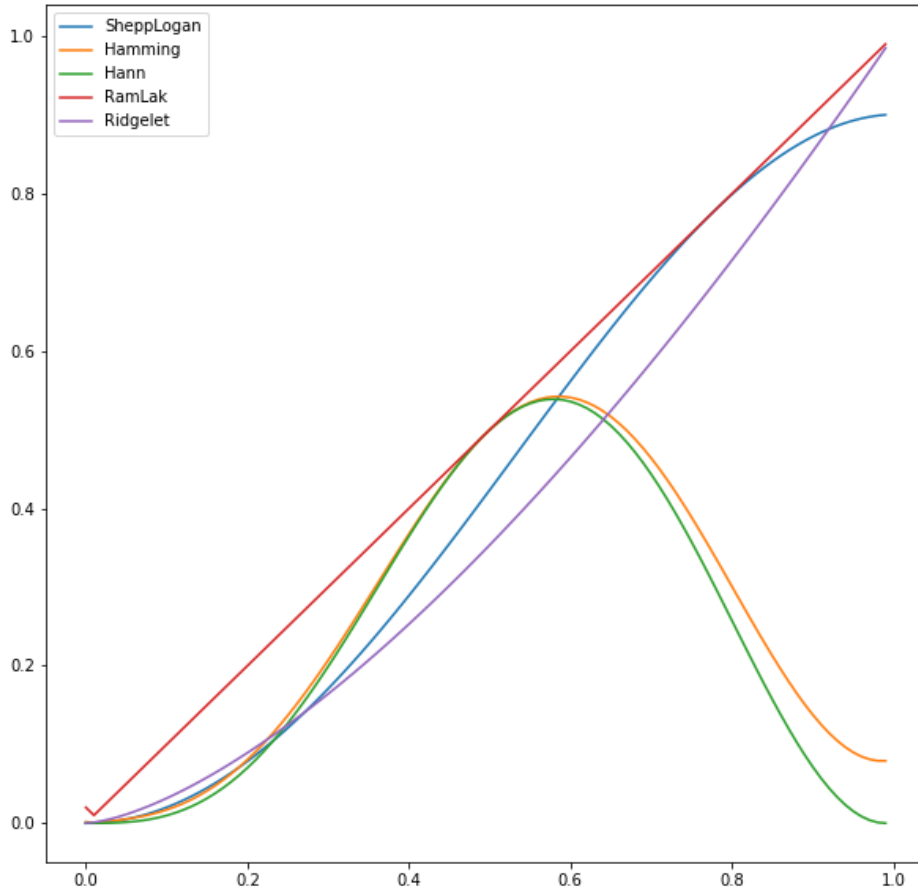
Figure D.1. Filters weight values.

E. Appendix E

The ideal J-PET scanner consists of single layer with radius of 43.73 cm. This layer is build from 384 scintillators with 50 cm length (See Figure E.1).
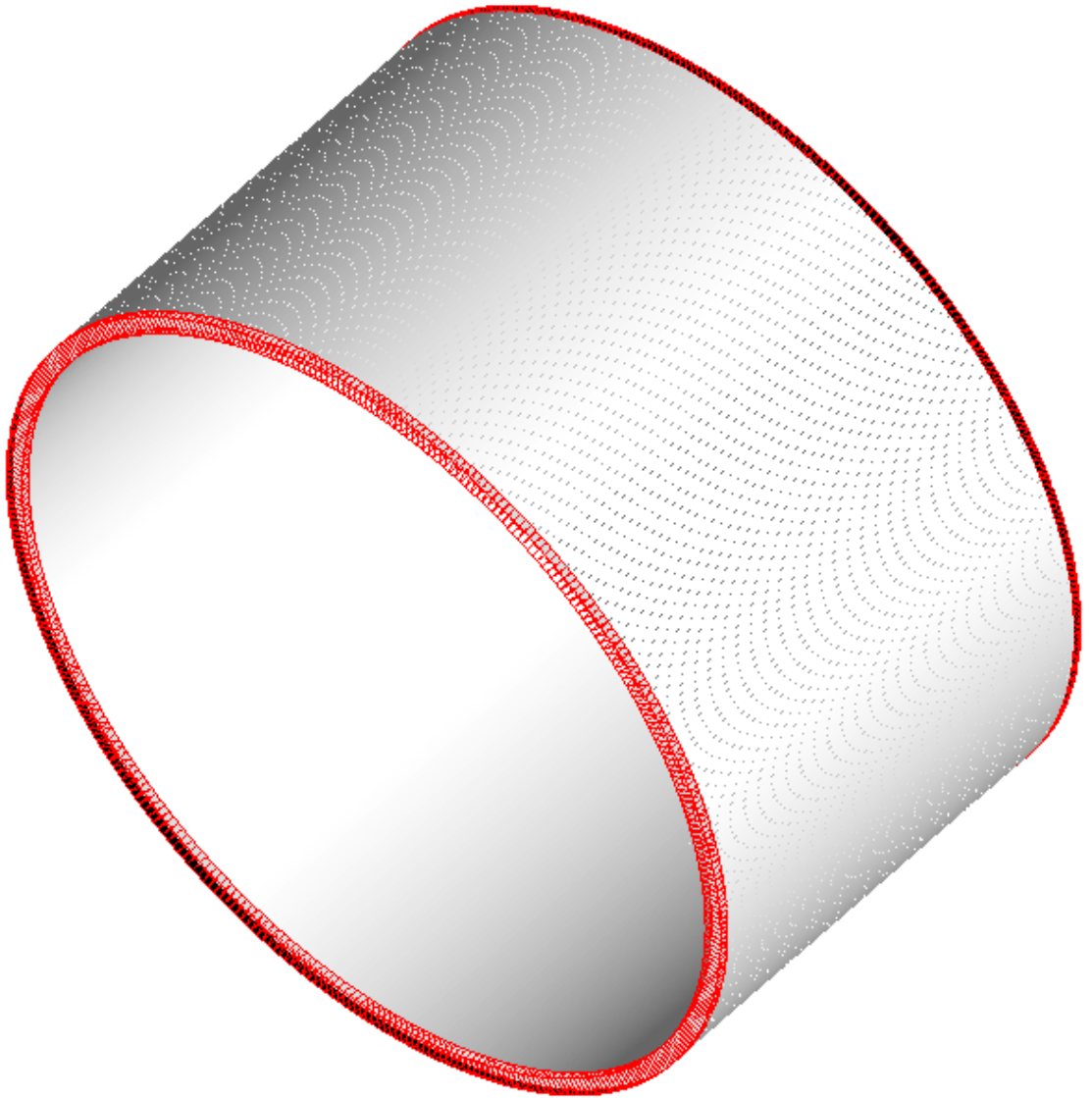
Figure E.1. Visualization of ideal J-PET scanner.